FISEVIER

Contents lists available at ScienceDirect

Acta Materialia

journal homepage: www.elsevier.com/locate/actamat



Full length article

In situ studies on irradiation resistance of nanoporous Au through temperature-jump tests



Jin Li a, b, C. Fan a, Q. Li a, H. Wang a, c, X. Zhang a, *

- ^a School of Materials Engineering, Purdue University, West Lafayette, IN 47907, USA
- ^b Department of Materials Science and Engineering, Texas A&M University, College Station, TX 77843-3123, USA
- ^c School of Electrical and Computer Engineering, Purdue University, West Lafayette, IN 47907, USA

ARTICLE INFO

Article history: Received 15 March 2017 Received in revised form 22 July 2017 Accepted 23 September 2017 Available online 25 September 2017

Keywords: In situ irradiation Nanoporous metals Temperature-dependent study Void swelling

ABSTRACT

Nanoporous materials have great potentials to alleviate irradiation-induced damage due to their giant surface-to-volume ratio. Previous *in situ* irradiation study on nanoporous Au at room temperature has shown the shrinkage of nanopores due to the absorption of irradiation-induced defects, and the shrinkage rate is pore-size-dependent. In this follow-up temperature-dependent study, we show that both defect density and nanopores evolve with irradiation temperature. Higher temperature results in lower defect density and reduced shrinkage rate of nanopores. The sink strength of nanopores as a function of temperature is estimated. Moreover, nanoporous Au exhibits significantly enhanced swelling resistance compared to coarse-grained Au. Potential mechanisms for temperature dependent irradiation resistance of nanoporous metals are discussed.

© 2017 Acta Materialia Inc. Published by Elsevier Ltd. All rights reserved.

1. Introduction

Irradiation responses of metallic materials subjected to highenergy particle (electron, neutron, and heavy ions) irradiation have been intensively investigated over the past few decades [1-4]. Next-generation nuclear reactors demand significant improvement of fuel performance as well as superior structural materials that can sustain extreme irradiation environment over a much longer period of service lifetime than those materials in conventional reactors [5,6]. Upon exposure to high-energy particle (neutron or heavy ions) bombardments, a significant number of point defects are produced in the irradiated materials [1,2]. Furthermore, these point defects can migrate, interact with other defects and evolve into much greater defect clusters, such as dislocation loops, dislocation networks and voids [7–9]. The microstructural damage can dramatically impact the properties and stability of irradiated materials in the form of irradiation-induced hardening and loss of ductility, change in material dimension (such as swelling), loss of electrical and thermal conductivities, and irradiation-induced phase segregation and precipitation, and degradation of corrosion resistance [2,10-18].

Among various types of irradiation-induced microstructural damage, volumetric swelling caused by the accumulation of voids is a severe problem [1,5,16,19-26]. Void swelling occurs in most irradiated metals and alloys [27,28]. It is very difficult to accommodate a swelling level up to 5% through engineering design. When swelling is larger than 10%, the materials suffer from severe irradiation embrittlement. Clearly, there is a strong need for the design of swelling-resistant structural materials. Void formation occurs due to the preferential absorption of interstitials by biased defect sinks [27], and typically requires two conditions: a supersaturation of vacancies; and agglomeration of vacancies before being annihilated by interstitials or defect sinks. If more vacancies than interstitials arrive at void nuclei, voids will grow continuously. One method to disrupt the formation and growth of voids is to introduce a high density of point defect sinks that can reduce the supersaturation and aggregation of vacancies.

To enhance irradiation resistance of materials, various types of defect sinks have been investigated, such as grain boundaries (GBs), twin boundaries (TBs), phase boundaries, etc. [29–41,79–81]. Nanoporous (NP) metals are expected to exhibit enhanced swelling resistance compared to their fully dense coarse-grained (CG) counterparts because of their large free surface area per unit volume [42–44]. An enlightening thought has been proposed nearly 40 years before to develop naturally porous structural materials in nuclear fuels to alleviate the fuel swelling caused by the

^{*} Corresponding author. E-mail address: xzhang98@purdue.edu (X. Zhang).

accumulation of fission gas [45]. However, the number of irradiation studies on NP metals remains very limited [44,46,47]. The potential of NP metals to alleviate void swelling has not been systematically testified yet. In our previous *in situ* irradiation study on NP Au, nanopore shrinkage has been observed instead of void swelling when irradiated at room temperature [46]. Nanopores shrink during irradiation by absorption of interstitials and their clusters, and their shrinkage rate is pore-size-dependent, i.e. smaller pores shrink faster because of higher efficiency to absorb irradiation-induced interstitials [46,48]. However, the irradiation response and swelling resistance of NP metals have not been investigated at elevated temperatures.

Defect sink strength is a parameter that quantifies the efficiency of a defect sink in annihilating irradiation-induced defects (or the affinity of a sink for defects), and it is one of the central parameters in the reaction-rate theory [49,50]. However, it remains challenging to obtain sink strength from experimental studies [51,52]. One method frequently used to study the sink strength of different GBs is to compare the width of the defect-denuded zones [53–56]. In parallel, computer simulations, such as molecular statics and molecular dynamics (MD) simulations are widely used to describe sink strength [51,55,57–61]. Most prior studies on sink strength focus on GBs, TBs or layer interfaces [55,61–64], while research on sink strength of free surface in NP metals remains limited.

Here we present a systematic study on *in situ* Kr ion irradiation on NP Au and CG Au at various temperatures. Temperature-dependent evolutions of defect size, density and diffusivities in both NP Au and CG Au have been investigated. Surprisingly, nanopore shrinkage in NP Au has been observed even close to peak swelling temperature, and the population of irradiation-induced voids in NP Au is largely reduced as compared to irradiated CG Au. Hypothetical mechanisms that lead to the suppression of void growth in NP Au are discussed. In addition, the sink strength of nanopores is calculated from experimental studies of NP Au.

2. Experimental

Recently, some methods have been reported to prepare NP Au [83–85]. In this study, Ag₆₅Au₃₅ (atomic ratio) leaves (procured from Co.) Central Art with dimensions 20 mm \times 20 mm \times 120 nm were sandwiched between two 304 stainless steel plates, and then cold rolled up to ~ 20% strain so as to reduce the foil thickness and achieve electron beam transparent specimens. After rolling, large pieces of the alloy films were peeled off from steel plates. Finally, these free-standing pieces of leaves (~100 nm) were chemically de-alloyed in a 70% HNO3 solution for 4 h at room temperature to remove Ag. The etched leaves were repeatedly rinsed in deionized water to remove residual acid and eventually lifted off by Cu grids (400 mesh) for in situ irradiation studies. More information on specimen preparation for transmission electron microscopy (TEM) experiment can be found elsewhere [46]. All specimens were investigated using a Thermo Fischer Scientific/ FEI Talos 200X and an FEI Tecnai G2 F20 ST microscope before and after irradiation. In situ irradiation experiment was performed at room temperature at the IVEM-TANDEM facility at Argonne National Laboratory. An 1 MeV Kr⁺⁺ ion beam was used for irradiation experiments to a maximum fluence of 2×10^{14} ions cm⁻² (~1 dpa). The dose rate applied during in situ irradiation experiments varied from 5×10^{-4} to 3.2×10^{-3} dpa/s. SRIM (Kinchin-Pease method) simulation was used to estimate the displacement damage profile (in the unit of displacements-per-atom (DPA)) and Kr ion distribution. Most Kr ions (99.99%) penetrated directly through the specimen and the residual Kr ion concentration in the TEM thin foil is ~0.01at.%. The temperature rise of specimens during in situ Kr ion irradiation measured by thermocouple is less than 10 °C.

3. Results

A bright-field TEM image in Fig. 1a showing the overview microstructure of NP Au before irradiation. The volume fraction of nanopores is 30 ± 15 vol%, and void-void distance is 50 nm. The average pore size is 30-40 nm. NP Au exhibits (110) texture as inferred from the inserted selected area diffraction (SAD) pattern. In this study, three series of *in situ* irradiation experiments are summarized in Fig. 1b.

Series I: temperature-jump tests ($400 \rightarrow 300 \rightarrow 200 \rightarrow 100$ °C, ~1 dpa at each temperature) for NP Au and CG Au;

Series II: in situ irradiation of NP Au at constant temperature, $200\,^{\circ}\text{C}$; and

Series III: in situ irradiation of NP Au and CG Au at room temperature (RT).

During irradiation, both NP Au and CG Au exhibit different responses at different temperatures. Fig. 2 compares irradiation responses of NP Au and CG Au at various temperatures through a series of transmission electron microscopy (TEM) snapshots obtained from *in situ* videos. Before irradiation, both CG Au and NP Au have little defects (Fig. 2a1-e1). During irradiation of CG Au at RT (Fig. 2a2-a4), defects accumulate rapidly with increasing dose to 1 dpa. At 400 °C, irradiation of CG Au induces much fewer defects (Fig. 2b2-b4). In comparison to irradiation of CG Au, during irradiation of NP Au at the same temperature (RT and 400 °C shown in Fig. 2c2-c4 and e2-e4), the number of defects increases gradually and moderately with dose up to 1 dpa. Furthermore, comparison of irradiation damage in NP Au at different temperatures (Fig. 2c-e) shows that defect density decreases with increasing irradiation temperature in NP Au.

SFTs are the major type of defect clusters introduced during irradiation. Bright-field TEM images in Fig. 3(a-c) shows that after temperature-jump irradiation tests of NP Au, $400 \rightarrow 100$ °C (to 5 dpa), many truncated SFTs are observed as confirmed by atomic resolution TEM. Irradiation of NP Au at a constant temperature (200 °C) to 2 dpa, (Fig. 3d-f) also leads to abundant SFTs. The statistics of defect size (cluster diameter) and density evolution as a function of dose and irradiation temperature in NP Au and CG Au are shown in Fig. 4. The colored background in (a-d) is used to distinguish different temperature stages for Series I specimens (irradiated at 400 \rightarrow 100 °C). The average defect size is ~4 nm after 0.1 dpa of irradiation of NP Au (Fig. 4a) regardless of irradiation temperature. In CG Au irradiated via temperature-jump tests, however, defect size increases from ~4 nm (irradiated at 400 °C) to 10 nm (at 100 °C) (Fig. 4b). At RT, the defect size in CG Au increases drastically before 0.1 dpa and then reaches a plateau, ~10 nm. During temperature-jump irradiation tests of NP Au, the defect density in Fig. 4c increases stepwise when irradiation temperature decreases from 400 to 100 °C. For isothermal irradiation of NP Au at 200 °C, defect density increases rapidly and reaches a saturation level comparable to that at 200 °C in the temperature-jump test. For irradiation performed at RT, the defect density increases much more rapidly to a greater level than that irradiated at 200 °C. The stepwise increase of defect density in CG Au shown in Fig. 4d is also observed during temperature-jump irradiation studies. Also the defect density in CG Au is 2-3 times larger than that in NP Au irradiated at the same condition. The saturation defect size in NP Au (Fig. 4e) is ~4 nm and has little temperature-dependence. In contrast in irradiated CG Au, saturation defect size is ~10 nm at RT, and decreases monotonically to ~4 nm with increasing temperature to 400 °C. Fig. 4f shows that saturation defect density in both NP Au and CG Au decreases gradually with increasing irradiation temperature. Defect cluster diffusivities (global and instantaneous) as a

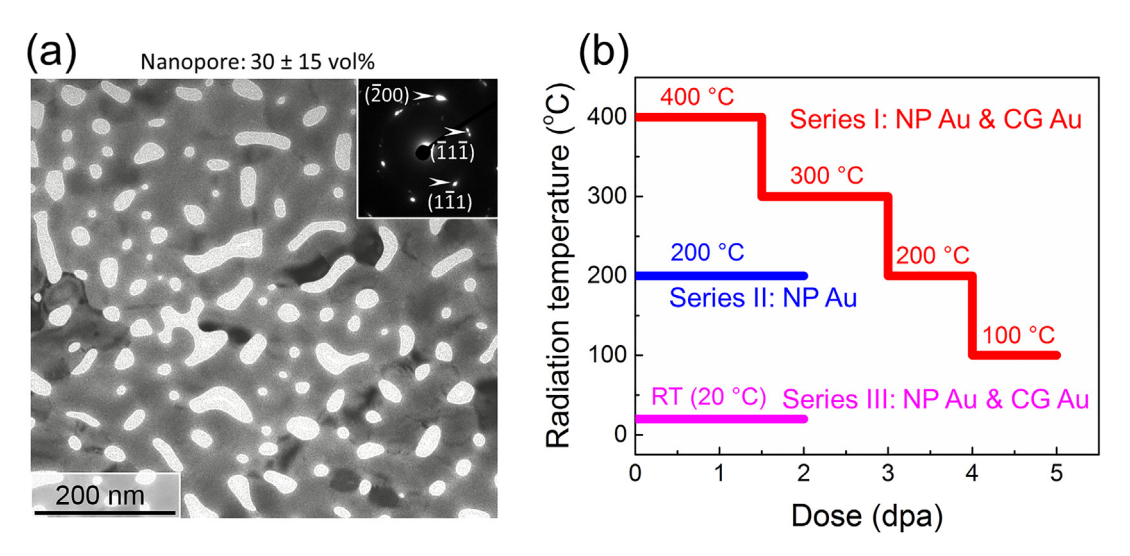


Fig. 1. (a) A bright-field TEM image showing the overview microstructure of NP Au before irradiation. The inserted SAD pattern shows NP Au exhibits (110) texture. (b) The summary of *in situ* irradiation experiments reported in this study. Series I: temperature-jump tests ($400 \rightarrow 300 \rightarrow 200 \rightarrow 100$ °C) for NP Au and CG Au; Series II: *in situ* irradiation of NP Au at constant 200 °C and Series III: *in situ* irradiation of NP Au at constant 200 °C and Series III: *in situ* irradiation of NP Au and CG Au at room temperature (RT).

function of irradiation temperature for Kr ion irradiated NP Au were also estimated. A defect's lifetime includes two components, defect migration time (hopping time) and dwelling time (rest time). To estimate the global diffusivity, both migration and dwelling time were taken into account. In contrast, when determining the instantaneous diffusivity, only a defect's migration time is considered. The global diffusivity of defect clusters, shown in Fig. 5a, increases significantly from 23 ± 5 to 48 ± 30 nm²/s when irradiation temperature increases from RT to 400 °C. The instantaneous diffusivity of defect clusters in Fig. 5b, however, shows little temperature dependence as compared to the global diffusivity.

The shrinkage of nanopores in NP Au has been observed at all irradiation temperatures explored in this study. At $100\,^{\circ}$ C, three nanopores in Fig. 6(a) with areas of 150, 380 and 290 nm² decrease their areas to 120, 310 and 230 nm², respectively after irradiation to 1 dpa (Fig. 6d), corresponding to 20%, 18.4% and 20.7% of reduction in volume. In comparison, three nanopores in Fig. 6e irradiated at $400\,^{\circ}$ C shrink by 2.5%, 6.3% and 1.3%, respectively. The statistics data derived from a series of nanopore shrinkage in NP Au irradiated at $100\,^{\circ}$ C are shown in Fig. 7a. The colored dash lines are the representative linear fitting results showing the reduction of pore areas. As shown in Fig. 7b, the average pore shrinkage rate (%/dpa) decreases monotonically with increasing irradiation temperature, from ~21%/dpa at RT [46] to 1.6%/dpa at $400\,^{\circ}$ C.

The shrinkage of nanopores is a consequence of the continuous migration of irradiation-induced defects towards nanopores. Representative defect capture events by an individual nanopore are shown in Fig. 8 for in situ irradiated NP Au at 200 °C over ~0.17 dpa (~53 s) (see Supplementary Video 1). A nanopore with an area of 430 nm² was monitored during irradiation (Fig. 8a). As the nanopore does not have perfect circular shape, its area rather than diameter is used for analysis. By 7.1 s, a defect cluster (outlined by olive dots) formed next to the nanopore (Fig. 8b). The defect cluster was then gradually absorbed by the nanopore (Fig. 8c-d). Two defect clusters outlined by blue dots were observed near the pore at 24.2 s (Fig. 8e). During irradiation, the smaller cluster gradually migrated towards the nanopore and combined with the large cluster (Fig. 8f-i), and the combined defect cluster was largely absorbed by the nanopore (Fig. 8j). A stacking fault tetrahedron (SFT) formed at 43.3 s (Fig. 8k). After 5.7 s, the SFT was destructed and partially removed, and then annihilated at 51.9 s (Fig. 8l-n). Fig. 80—p show, by 53 s, a large defect cluster emerged adjacent to the nanopore and was instantly eliminated within 0.2 s. During the interaction of these defect clusters with the nanopore, the area of the nanopore reduced from 430 to 420 nm².

Supplementary video related to this article can be found at https://doi.org/10.1016/j.actamat.2017.09.054.

Void swelling is, in general, expected in FCC metals under irradiation near peak swelling temperature, ~250 °C for Au. The comparison of void swelling behavior between NP Au and CG Au in Series I study (temperature-jump test) after irradiation to 5 dpa is shown in Fig. 9. In CG Au as shown in Fig. 9a, nanovoids form with a density of $9.6 \pm 2.2~(\times 10^{21}/m^3)$. In comparison, in irradiated NP Au (Fig. 9b), the irradiation-induced nanovoids have a lower density of $1.1 \pm 0.5~(\times 10^{21}/m^3)$. The statistic distributions in Fig. 9c and d show that the average void size in irradiated CG and NP Au is $5 \pm 3~\text{nm}$, and $2 \pm 1~\text{nm}$, respectively. The irradiated CG Au has a maximum void size of 12 nm, comparing to a maximum void size of 4 nm in irradiated NP Au.

Defect sink strength is an important parameter that quantifies the efficiency of a defect sink in annihilating irradiation-induced defects. Fig. 10a shows the number of defects being absorbed by the free surface of nanopores $(\rho_{\rm absorb}^{\rm NP})$ as a function of irradiation temperature. The results are deduced from Fig. 4f by subtracting the defect density in NP Au from the defect density in CG Au irradiated at the same temperature. Below 200 °C, $\rho_{\rm absorb}^{\rm NP}$ decreases slightly (from 11.5 to 10.5 \times 10 $^{22}/{\rm m}^3$) with increasing temperature. However, when T > 200 °C, $\rho_{\rm absorb}^{\rm NP}$ decreases sharply. The calculated nanopore sink strength as a function of irradiation temperature is shown in Fig. 10b. The shadow area represents the deviation by considering the variation of nanopore size. Clearly, two distinct regions can be identified. Below 200 °C (Region I), sink strength shows little temperature dependence, whilst above 200 °C (Region II), sink strength is inversely proportional to the irradiation temperature.

4. Discussion

4.1. Defects in irradiated NP Au

In NP Au irradiated at different temperatures, a large number of

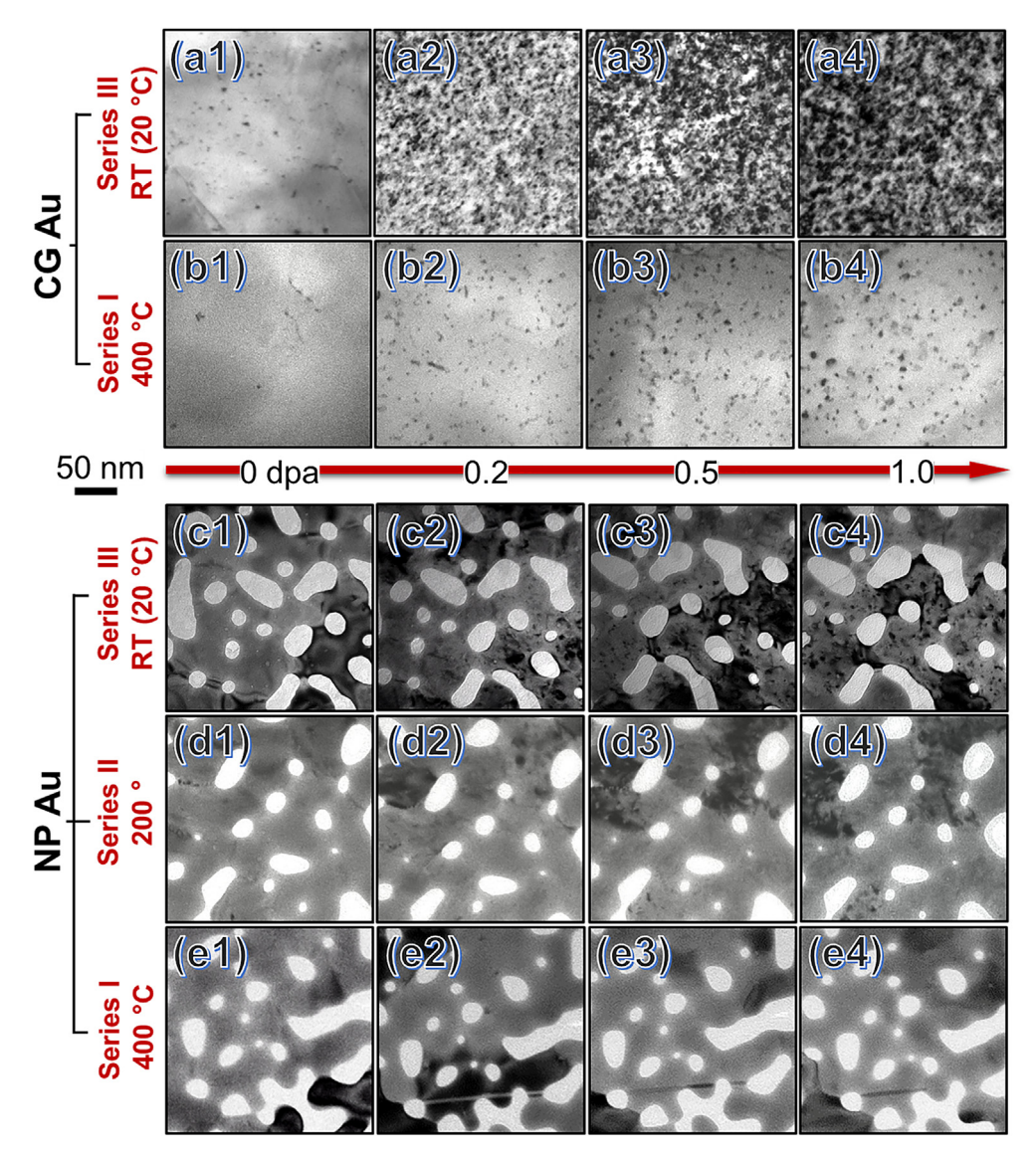


Fig. 2. Transmission electron microscopy (TEM) snapshots obtained from *in situ* Kr ion irradiation videos compare irradiation response between NP Au and CG Au at various irradiation temperatures. Before irradiation, both CG and NP Au had little defects (a1, b1, c1, d1, e1). (a2–a4) During irradiation, defects accumulated rapidly in CG Au at RT (b2–b4). At 400 °C, irradiation induced much fewer defects in CG Au (c2-c4, d2-d4, e2-e4). In contrast, during irradiation of NP Au, the number of defects increased gradually and moderately with dose up to 1 dpa. Furthermore, defect density decreased with increasing irradiation temperature.

SFTs are observed. SFTs are known to have distinct triangular shapes (complete or truncated as can be seen from the atomic-resolution TEM images in Fig. 3) and are considered to be the most energetically favorable configuration compared to faulted and perfect loops when defect cluster size is small [7]. The formation of SFTs relies on three different mechanisms. (1) Direct formation from the vacancy rich cascade during energetic displacement [1,65,66]. (2) The classic Silcox-Hirsch mechanism where SFTs form from equilateral triangular vacancy Frank loops by dissociation [67,68]. However, it is less likely that SFTs are created from equilateral triangular vacancy Frank loops in the real irradiation cascade. Therefore, another SFT formation mechanism has been proposed that is (3) evolution from the scalene hexagonal vacancy Frank loops [69].

Besides SFTs, a large number of interstitial clusters form during irradiation. These perfect interstitial loops typically have Burgers vector of a/2 $\langle 110 \rangle$ on either $\{110\}$ or $\{111\}$ planes and are usually mobile, while faulted interstitial loops $(a/6 < 112 > \{111\})$ and vacancy clusters (vacancy loops and SFTs) are immobile [70]. A

majority of the glissile defect clusters in Au are perfect interstitial loops.

In addition, since irradiation has been performed from RT to 400 °C in this study, temperature (T) effect should also be considered when discussing the nature of irradiation-induced defects. Based on the one-interstitial model [71], Stage III temperature, which is RT for Au, corresponds to the onset of vacancy motion. Stage V temperature, ~250 °C, is correlated to the thermal dissociation of vacancy clusters [1,72]. Therefore, the current irradiation experiments can be divided into two groups. The first group refers to irradiation from RT to 200 °C. At this temperature range, because most of the vacancies are tied up in sessile vacancy clusters, a majority of observed mobile dislocation loops in Au are of the interstitial type, SFTs are a dominant vacancy type of defects, and void nucleation and growth is strongly suppressed. Hashimoto et al. have shown that approximately 90% of irradiation-induced defects near 80 °C are SFTs in Cu [73] and other FCC systems [74-76]. For the second group (T > Stage V, greater than 200 °C), since SFTs are thermally unstable, the predominant visible features are interstitial

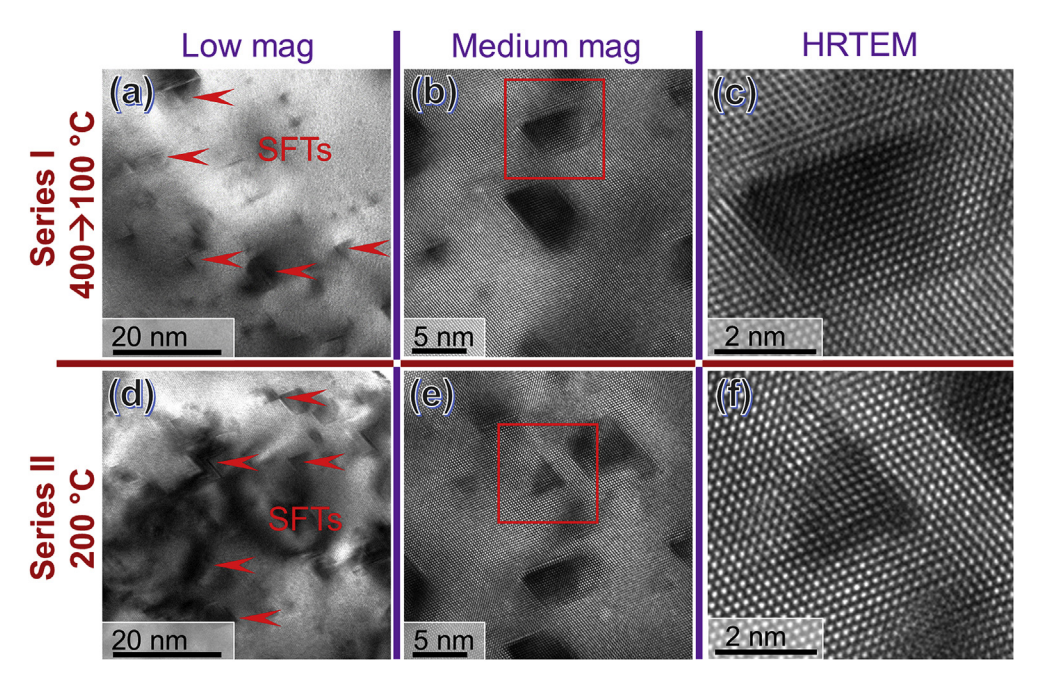


Fig. 3. Bright-field TEM images are showing the formation of SFTs in irradiated NP Au. (a–c) After temperature-jump irradiation, $400 \rightarrow 100$ °C (5 dpa), SFTs (many of them are truncated) are observed as confirmed by their triangular shape and atomic resolution TEM. (d–f) Irradiation at 200 °C (2 dpa) also leads to abundant SFTs.

loops and the coexistence of SFTs and voids, and voids become dominating defects as the dose increases [77].

4.2. Defect evolution (size/density) as a function of dose and temperature

Defect net concentration is a result of the balance between defect production (dose-rate dependent), absorption (sink dominated) and recombination (irradiation temperature dominated). When NP Au and CG Au are irradiated at the same temperature and dose-rate, the generation and recombination of defects are nearly identical in the two cases. However, since NP Au has a much higher density of defect sinks (nanopores), the net concentration of defects is much lower in NP Au compared to CG Au irradiated at the same condition.

Statistical data in Fig. 4 present more details on the defect size and density evolutions as a function of dose and temperature. Limited by 2D images, the longest dimension of each defect was measured. Thus, the measured defect size represents an upper bound. In comparison, defect density analysis reflects the lower bound since not all defects can be resolved under *in situ* TEM observation. Several remarkable phenomena are worth mentioning.

- 1. Defect size and density are smaller in NP Au than those in CG Au at almost all irradiation conditions.
- 2. Defect size in NP Au reaches a plateau quickly after ~0.3 dpa regardless of irradiation temperature, while in CG Au, defect size decreased drastically at higher irradiation temperatures.
- 3. Defect density decreases with increasing temperature in both NP Au and CG Au.
- 4. The NPAu irradiated at 200 $^{\circ}$ C (Series II) exhibits nearly identical saturation defect size and density compared to the NPAu irradiated during the 200 $^{\circ}$ C stage of temperature jump test (Series I).

Due to the existence of high-density nanopores, NP Au typically

has both smaller defect size and lower defect density than those in CG Au. However, there is an interesting exception: defect size in NP Au and CG Au irradiated at 400 °C is similar, ~4 nm. One possible reason for such an exception is that at 400 °C, the growth of defect clusters becomes very difficult due to an active thermal vacancy-interstitial recombination process. During irradiation at RT, the defect size in CG Au grows to 10 nm, whereas defect size in NP Au irradiated at the same condition remains 4 nm. The free surface of nanopores in NP Au clearly inhibits the growth of defects in NP Au by absorbing both vacancies and interstitials.

As mentioned earlier (point 4), defect size and density obtained via temperature-jump irradiation tests are similar to those irradiated at different temperatures separately. Therefore, temperature-jump tests may provide an efficient way to investigate defect evolution comparing with a series of stand-alone solo-temperature irradiation experiments. It should be noticed that temperature-jump tests performed in decremented temperature steps may be more appropriate to investigate temperature dependent studies, as defect generation is an instantaneous event, but defect annihilation requires much longer time. Therefore, if the temperature-jump experiment was carried out in an opposite way (incremental temperature steps), the defects formed at a lower temperature stage may survive irradiation at the following stages, compromising the quantification of defect accumulations at higher irradiation temperatures.

4.3. Temperature-dependent diffusivities of defect clusters

Defect migration kinetics, which is crucial for the modeling of defect evolution in irradiated metals, remains largely unknown [78]. Our previous study has reported the influence of dose-rate on global and instantaneous diffusivities of defect clusters in Kr ion irradiated NP Au at RT [46]. It was found that the global diffusivity of defect clusters (at RT) is significantly reduced when the dose rate decreases, while the instantaneous diffusivity has little dependence on dose rate. The potential mechanisms are interpreted from the aspects of defect diffusion distance and defect lifetime. In the

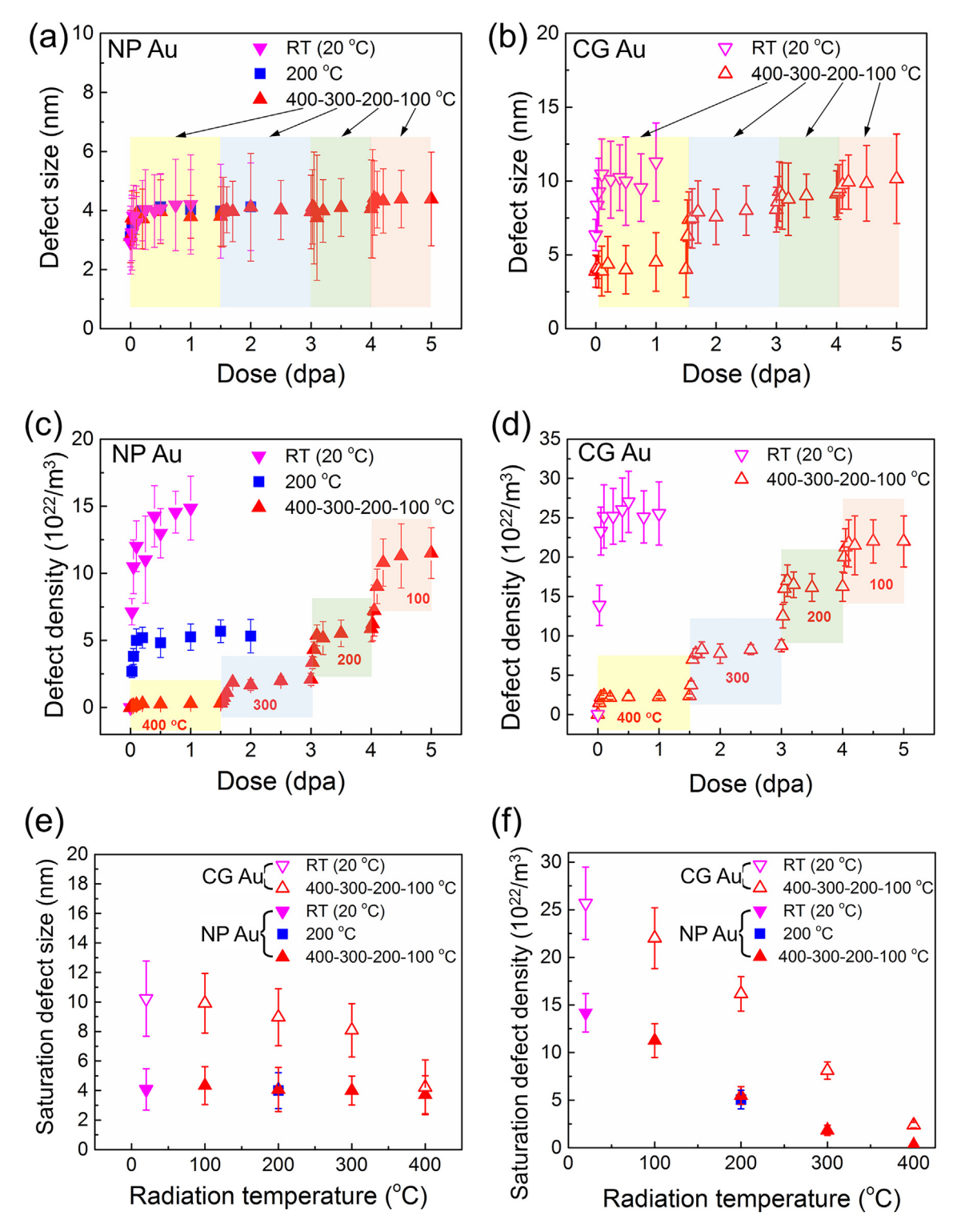


Fig. 4. Statistics of defect size (cluster diameter) and density evolution as a function of dose (a-d) and irradiation temperature (e-f) in NP Au and CG Au. The colored background in (a-d) is used to distinguish different temperature stages for Series I specimens (irradiated at $400 \rightarrow 100$ °C). (a) The average defect size is ~4 nm after 0.1 dpa for NP Au regardless of irradiation temperature. (b) In CG Au irradiated via temperature-jump tests, defect size increases from ~4 nm (irradiated at 400 °C) to ~10 nm (at 100 °C). At RT [46], the defect size in CG Au increases drastically before 0.1 dpa and then reaches a plateau, ~10 nm. (c) During temperature-jump irradiation tests of NP Au, the defect density increases stepwise when irradiation temperature decreases from 400 to 100 °C. For isothermal irradiation of NP Au at 200 °C, defect density increases rapidly and reach a saturation level comparable to that at 200 °C in the temperature-jump test. For irradiation performed at RT [46], the defect density increases much more rapidly to a greater level than that irradiated at 200 °C. (d) The stepwise increase of defect density in CG Au was also observed during temperature-jump irradiation studies. Also, the defect density in CG Au is 2-3 times larger than that in NP Au irradiated at the same condition. (e) The saturation defect size in NP Au is ~4 nm and has little temperature-dependence. In contrast in irradiated CG Au, saturation defect size is ~10 nm at RT, and decreases monotonically to ~4 nm with increasing temperature to 400 °C. (f) Saturation defect density in both NP Au and CG Au decreases gradually with increasing irradiation temperature. (For interpretation of the references to colour in this figure legend, the reader is referred to the web version of this article.)

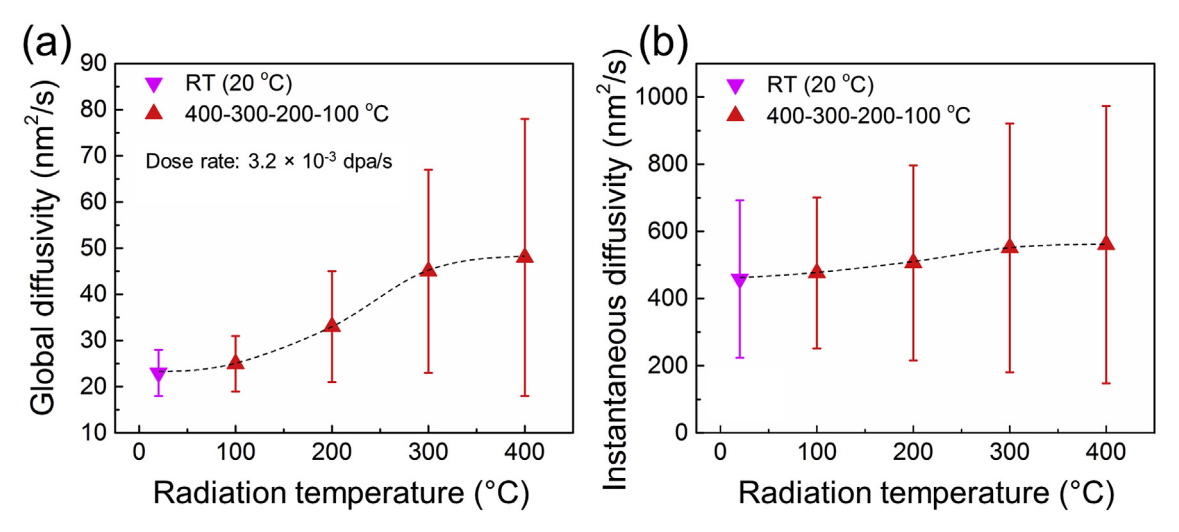


Fig. 5. Defect cluster diffusivities as a function of irradiation temperature for Kr ion irradiated NP Au. (a) The global diffusivity of defect clusters increases significantly from 23 ± 5 to $48 \pm 30 \text{ nm}^2/\text{s}$ when irradiation temperature increases from RT [46] to $400 \,^{\circ}\text{C}$. (b) The instantaneous diffusivity of defect clusters shows little temperature dependence as compared to the global diffusivity.

current study, temperature-dependent global and instantaneous diffusivities of defect clusters for NP Au are investigated. The estimation of diffusivities is very difficult for CG Au because the film was damaged by ion beam very rapidly. Thus, the migration of single defect clusters in CG Au can be barely traced. For NP Au, The global diffusivity of defect clusters in NP Au increases prominently from 23 \pm 5 to 48 \pm 30 nm²/s, when irradiation temperature increases from RT to 400 °C. The rapid increase of global diffusivity is due to the decrease in defect density at higher irradiation temperature, which in turn affects the migration distance of defect clusters. In general, a lower defect density leads to longer migration distance, hence greater diffusivity. The error bar of global diffusivity also increases with increasing temperature. This can also be ascribed to defect density. Since the number of defects is very low at high temperature, a defect cluster can migrate over a long distance without being arrested. However, because the existence of high-density nanopores, the defect migration distance is largely determined by the defect-to-pore distance (or defect-sink distance). If a defect is close to a nanopore, then it can only migrate over a short distance before being annihilated, and vice versa. Therefore, the calculated global diffusivity varies in a wide range depending on the defect-to-pore distance.

It is intriguing to observe that the instantaneous diffusivity of defect clusters in NP Au shows very limited temperature dependence, $476 \pm 225 \text{ nm}^2/\text{s}$ at RT vs. $560 \pm 412 \text{ nm}^2/\text{s}$ at $400 \,^{\circ}\text{C}$. Although the fundamental mechanisms behind such a phenomenon remain unclear, we hypothesize that the such a weak temperature dependence may be related to the defect-sink separation distance. The instantaneous diffusivity of a defect cluster is largely determined by the distance of a single "jump" between two defect clusters or between defect and sink (nanopores). At 200 $^{\circ}\text{C}$, the distance between two defects is ~25 nm, and such a distance

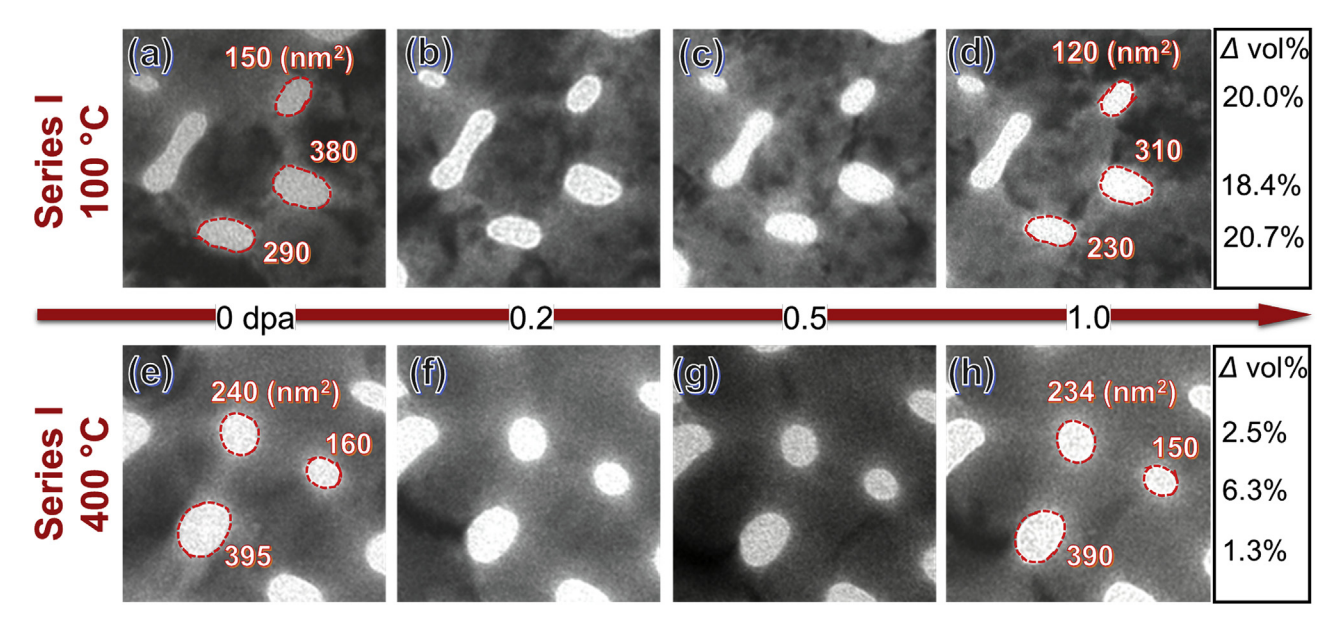


Fig. 6. In situ video snapshots showing the comparison of pore shrinkage of NP Au at two different temperatures. (a–d) At 100 °C, three nanopores with areas of 150, 380 and 290 nm² decreases to 120, 310 and 230 nm², respectively after irradiation to 1 dpa, corresponding to 20%, 18.4% and 20.7% reduction in volume. (e–h) In comparison, three nanopores barely shrink at 400 °C, by 2.5%, 6.3% and 1.3%, respectively.

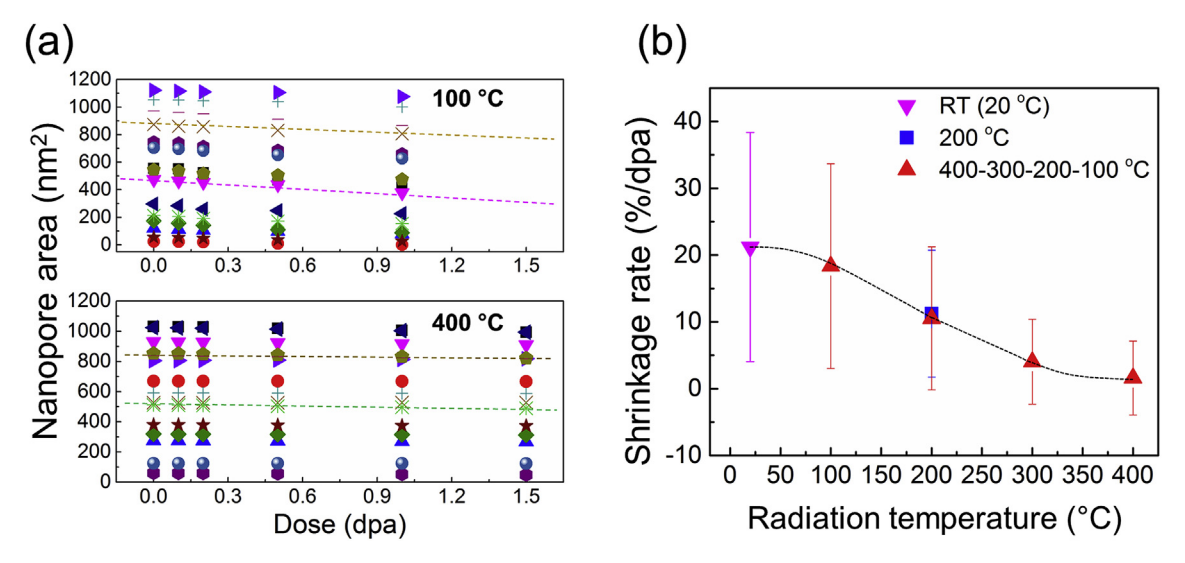


Fig. 7. Statistic data reveal the temperature-dependent shrinkage of nanopores during irradiation of NP Au. (a) Two examples of NP Au irradiated at 100 and 400 °C showing the evolution of pore area versus irradiation dose. The color-dashed lines are the representative linear fitting results. (b) Average pore shrinkage rate (%/dpa) decreases with increasing irradiation temperature, from ~21%/dpa at RT [46] to 1.6%/dpa at 400 °C. (For interpretation of the references to colour in this figure legend, the reader is referred to the web version of this article.)

increases to 70 nm at 400 $^{\circ}$ C due to reduced defect density. The average pore-to-pore separation distance in NP Au is ~50 nm. Assume a defect cluster is located between two nanopores, then the defect-to-pore distance is ~25 nm, which is equal to the defect-defect separation distance at 200 $^{\circ}$ C.

4.4. Calculation of free surface (nanopores in NP Au) sink strength

Defect sink strength (with a unit of cm $^{-2}$) is a key parameter in the reaction-rate theory to quantify the efficiency in annihilating irradiation-induced defects. The defect sink strength is in general calculated computationally. Experimentally, the estimation of sink strength can be obtained from the comparison studies between nanostructured materials and their CG counterparts. In this case, Series I NP Au and CG Au are both irradiated at the same conditions with different temperatures. The total number of defects, $\rho_{\rm total}$, that is estimated from experimental observations can be written as:

$$\rho_{\rm total}^{\rm NP~Au} = \rho_{\rm gen} - \rho_{\rm recom} - \rho_{\rm absorb}^{\rm Sur} - \rho_{\rm absorb}^{\rm NP}, \tag{1}$$

and

$$\rho_{\text{total}}^{\text{CG Au}} = \rho_{\text{gen}} - \rho_{\text{recom}} - \rho_{\text{absorb}}^{\text{Sur}}, \tag{2}$$

where $\rho_{\rm gen}$ is the number of defects generated under irradiation and $\rho_{\rm recom}$ is the number of defects annihilated through recombination. $\rho_{\rm absorb}^{\rm Sur}$ and $\rho_{\rm absorb}^{\rm NP}$ are the number of defect absorbed by film upper/lower surfaces and nanopores, respectively. Since the irradiation conditions are kept the same and TEM specimens have the identical thickness for NP Au and CG Au, $\rho_{\rm gen}$, $\rho_{\rm recom}$, and $\rho_{\rm absorb}^{\rm Sur}$ are nearly the same in the two equations. In addition, since the average grain size in both NP Au and CG Au are both very large (on the order of microns), defect absorption through GBs is negligible. In Eqs. (1) and (2), the only different term is the number of defects annihilated by nanopores, $\rho_{\rm absorb}^{\rm NP}$. Fig. 10a shows the calculated $\rho_{\rm absorb}^{\rm NP}$ as a function of temperature. Below 200 °C, $\rho_{\rm absorb}^{\rm NP}$ varies very little from 10.5 to 11.5 (\times 10²²/m³). However, a turning point exists at ~200 °C, after which $\rho_{\rm absorb}^{\rm NP}$ decreases quickly with increasing temperature. Note that, this temperature is similar to the thermal dissociation

temperature for sessile vacancy clusters (Stage V temperature of defect recovery) in Au [1,72]. After dissociation, vacancies continuously recombine with interstitials, and the number of defect clusters that migrate (absorb) to nanopores decreases. Therefore, it is reconcilable to see $\rho_{\rm absorb}^{\rm NP}$ decreases more rapidly at higher temperatures.

 $ho_{
m absorb}^{
m NP}$ obtained based on foregoing analysis provides an important parameter in calculating sink strength for nanopores in NP Au. Assuming the nanopore density is $ho_{
m V}$ (cm $^{-2}$), film thickness is h and nanopores exhibit cylindrical shape with the volume-equivalent radius of R, at a given area, A, a measure of the effective sink strength of nanopores, $K_{
m NP}$, the total number of defects absorbed by the inner surface (free surface) of nanopores (per cm 2), can be calculated as:

$$K_{NP} = \frac{A \cdot h \cdot \rho_{absorb}^{NP}}{2\pi R \cdot h \cdot \rho_{V} \cdot A} = \frac{\rho_{absorb}^{NP}}{2\pi R \cdot \rho_{V}}.$$
 (3)

The value of ρ_{absorb}^{NP} is shown in Fig. 10a, and the volume-equivalent radius, R, and density, ρ_{v} , are estimated to be 11 ± 5 nm and 3.1×10^{10} cm $^{-2}$, respectively. The calculated effective sink strength of nanopores, K_{NP}, as a function of temperature is shown in Fig. 10b. The shadowed area represents the deviation by considering the size distribution of nanopores. Two distinct regions can be identified in the plot. When temperature is below 200 °C. which is Region I, effective sink strength shows little temperature dependence. In this case, defect sinks play a dominating role in eliminating irradiation-induced defects compared to thermal recombination, because temperature is not high enough to trigger massive defect recombination. Hence the measured effective sink strength at room temperature in the current study may approach the inherent sink strength of nanopores. In Region II ($T > 200 \, ^{\circ}C$), however, the calculated effective sink strength decreases rapidly. The effect of defect sinks in this case is less pronounced because of the much greater thermal recombination rate. It is worth mentioning that the result does not necessarily indicate that real (inherent) sink strength decreases at elevated temperature.

The strategy discussed previously makes the quantification of effective sink strength possible in nanostructured materials. However, several factors shall be considered. First, the effective sink

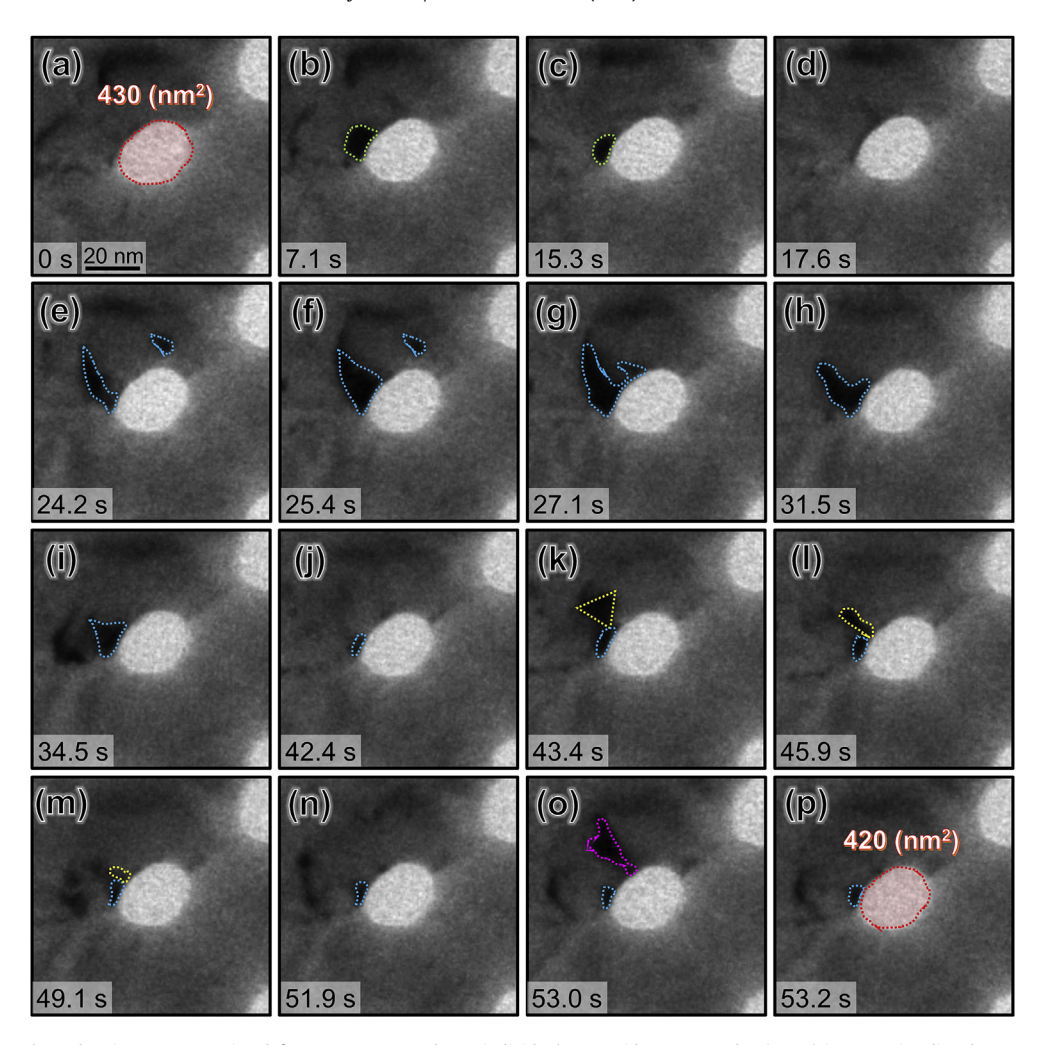


Fig. 8. In situ video snapshots showing representative defect capture events by an individual nanovoid over ~0.17 dpa (~53 s) in NP Au irradiated at 200 °C (see Supplementary Video 1). (a) A nanopore with an area of 430 nm² was monitored during irradiation. (b) A defect cluster (outlined by olive dots) formed next to the nanopore after 7.1 s. (c-d) The defect cluster was gradually absorbed by the nanopore. (e-j) Two defect clusters outlined by blue dots were observed at 24.2 s. During irradiation, the smaller cluster gradually migrated towards the nanopore, and the larger cluster continuously grew. Finally, the two clusters combined and were mostly absorbed by the nanopore. (k) A stacking fault tetrahedron (SFT) formed at 43.3 s. (l-n) After 5.7 s, the SFT was destructed and partially removed, and then annihilated at 51.9 s. (o-p) By 53 s, a large defect cluster emerged adjacent to the nanopore and was immediately eliminated within 0.2 s. Due to the absorption of defect clusters during irradiation, the area of the nanopore reduced from 430 to 420 nm². (For interpretation of the references to colour in this figure legend, the reader is referred to the web version of this article.)

strength calculated here considers mostly defect clusters rather than point defects that are captured by sinks. Thus, we may have underestimated the effective sink strength of nanopores. Second, the results indicate that the effective sink strength may not depend on the dose level, but rather on dose-rate. More defects can be produced at higher dose-rates, and therefore, the effective sink strength increases as more defects may be captured by sinks. Malerba et al. pointed out that the sink strength not only depends on the type, shape, and size of the sinks but also depends on the dimensionality of the motion of the affected migrating species [58]. Nevertheless, it is not clear from the present study if the effective sink strength saturates upon a certain dose-rate. Further studies are necessary to answer this question. The method provided in this study offers an opportunity to compare sink strength for different types of defect sinks under the same irradiation condition.

4.5. Nanopore shrinkage and suppressed void swelling in NP Au

As mentioned earlier, our previous studies on NP Au have shown that nanopore shrinkage occurred at RT and no irradiation-induced voids were detected [82]. In the current study, nanopore shrinkage

has been identified again in NP Au at all irradiation temperatures, including the peak swelling temperature for Au. The shrinkage rate of nanopores decreases with increasing irradiation temperature (Fig. 7b). One may envision that the growth of nanopores is due to the arrival of vacancies. For Au irradiated at room temperature most vacancies are tied up in sessile vacancy clusters (SFTs, vacancy loops) formed directly in the displacement cascades. Consequently, the mobility of vacancies and the void nucleation and growth are strongly suppressed. Thus, more interstitials arrive at nanopores, leading to the shrinkage of nanopores. At higher irradiation temperature, the mobility of vacancies increases, and the recombination rate between interstitials (and clusters) and vacancies (and clusters) increases. Because nanopores absorb fewer defects at elevated temperatures, the nanopore shrinkage rate decreases. No obvious growth of nanopores was observed at high temperatures.

In addition to nanopore shrinkage, void swelling is observed in Series I CG Au after irradiation up to 5 dpa, while both size and density of irradiation-induced voids are remarkably reduced in NP Au (Fig. 9). Many voids in irradiated CG Au are larger than 4 nm and the maximum size is 12 nm, while most of the voids in NP Au are smaller than 3 nm and the maximum size is 4 nm. Comparing to

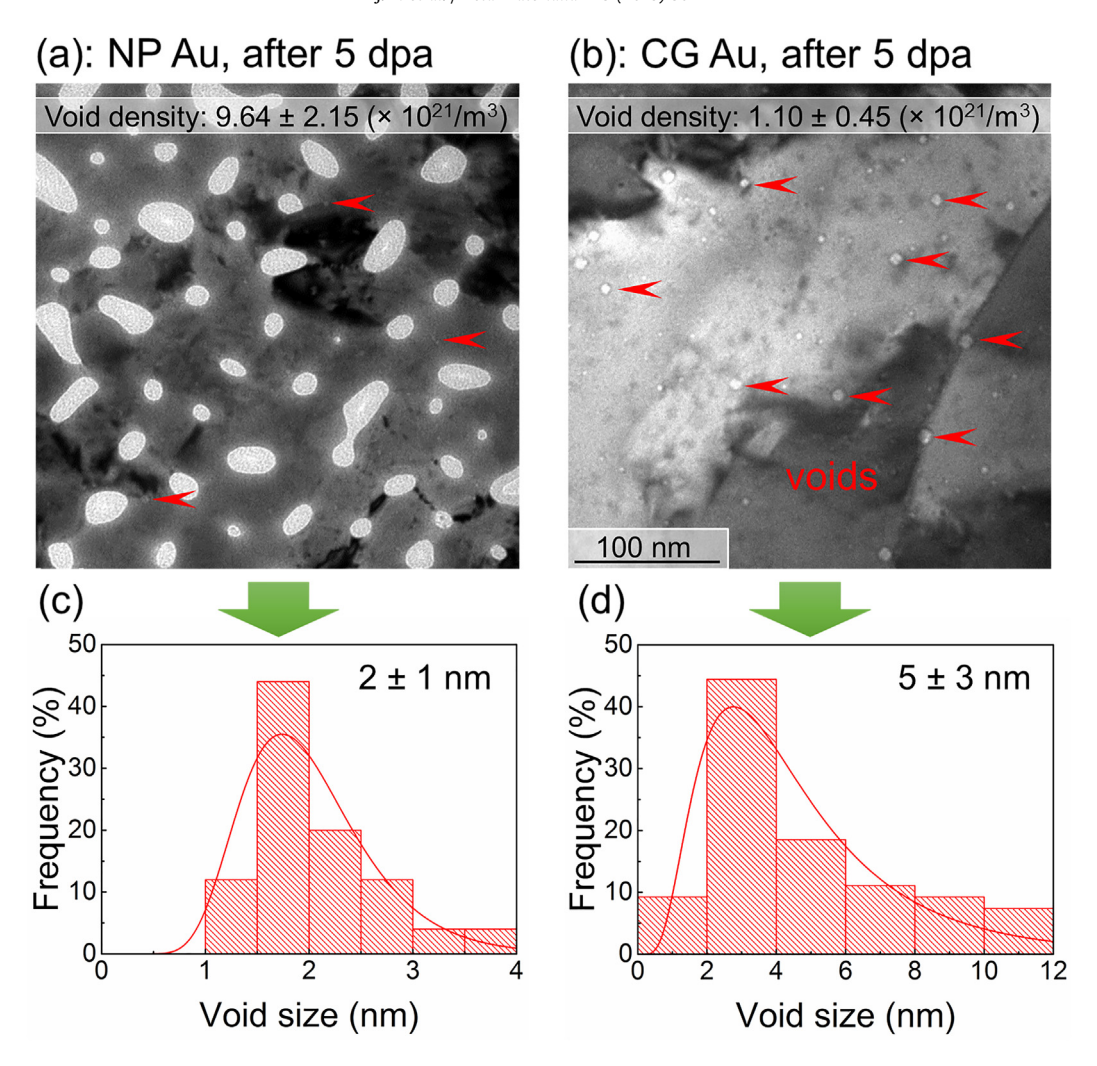


Fig. 9. Comparison of void swelling between NP Au and CG Au in Series I study (temperature-jump test) after irradiation to 5 dpa. (a) In CG Au, irradiation-induced nanovoids have a density of $9.6 \pm 2.2 \, (\times 10^{21}/\mathrm{m}^3)$. (b) In comparison, in irradiated NP Au, the irradiation-induced nanovoids have a density of $1.1 \pm 0.5 \, (\times 10^{21}/\mathrm{m}^3)$. (c) The statistics distribution shows that the average void size is 5 ± 3 nm. (d) The average void size in irradiated NP Au is 2 ± 1 nm. The irradiated CG Au has a maximum void size of 12 nm, comparing to 4 nm in irradiated NP Au.

irradiated CG Au, the void size is more than two times smaller, and the void density is reduced by almost an order of magnitude in the irradiated NP Au. It is worth mentioning that nanopore shrinkage could be the considered as negative swelling (densification) and the magnitude of volume reduction induced by nanopore shrinkage is much larger than the volume expansion due to irradiation induced voids in NP Au at elevated temperatures. In addition, the volume of irradiation-induced voids in NP Au is nearly two orders of magnitude lower than that in irradiated CG Au. Hence, NP Au exhibits prominently improved swelling resistance.

Schematics in Fig. 11 illustrate the hypothetical mechanisms of void formation and nanopore shrinkage in NP Au and CG Au at different temperatures during irradiation. Same amount of interstitials and vacancies are created in a given volume in both NP Au and CG Au during irradiation. However, in CG Au (Fig. 11a), interstitials continuously migrate towards film upper and lower film surfaces (GBs contribution is not considered because of the giant grain size compared to film thickness), and most of the vacancies are left behind. Therefore, interstitials have medium concentration, and vacancies exhibit high concentration. At high temperature, vacancies become mobile and agglomerate to form large clusters, and finally, transform into voids. Because of high supersaturated

vacancy concentration, voids grow rapidly in terms of both size and density. In contrast in NP Au irradiated at high temperatures (Fig. 11b), due to the existence of nanopores, both interstitials and vacancies will be trapped by nanopores. Consequently, interstitials exhibit low concentration, and vacancies have medium concentration compared to that in CG Au. In this case, only small vacancy clusters can form, and those clusters eventually evolve into small voids. Compare to irradiation of NP Au at low temperatures (Fig. 11c), nanopores shrink at much slower rates at high temperatures due to two major reasons: (1) accelerated thermal recombination of opposite point defects at high temperature, and (2) the increasing mobility of vacancies at high temperature. Consequently, fewer interstitial-type defects can reach nanopores before being annihilated by vacancy-type defects, and the preferential absorption of interstitial-type defects by nanopores is interrupted because vacancy-type defects could also reach to nanopores. Therefore, nanopore shrinkage rate decreases at high temperature. Since void nucleation and growth are largely suppressed at low temperature, little void swelling occurs in (c). Noted that three other factors related to interstitials are intentionally not shown in the schematics for clarity: (1) interstitial annihilation due to pre-existing defects, such as dislocations; (2) the migration of interstitial to film surface;

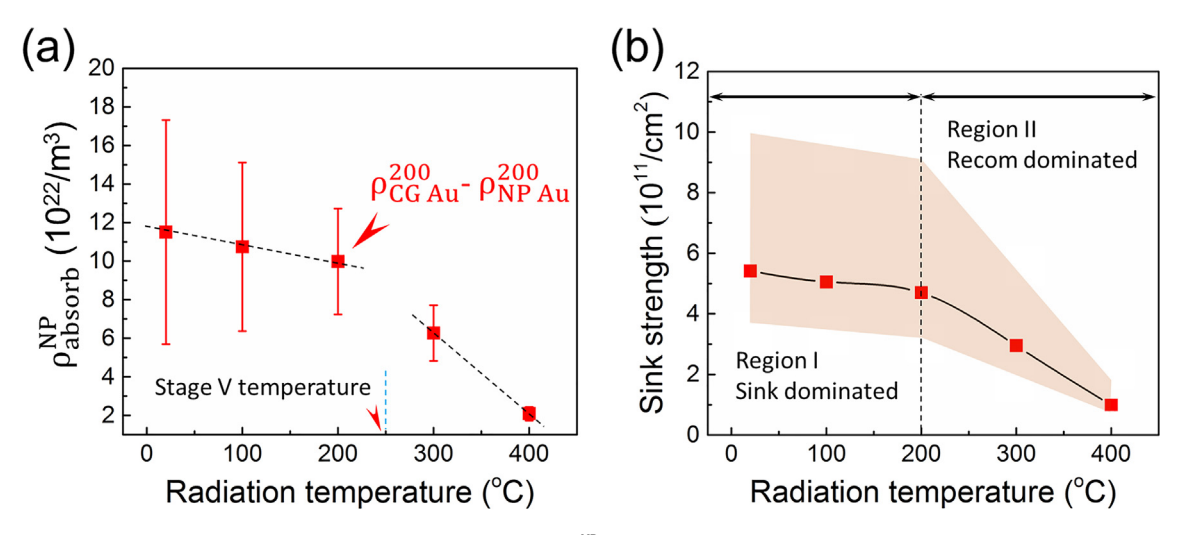


Fig. 10. (a) The number of defects being absorbed by the free surface of nanopores ($\rho_{\rm absorb}^{\rm NP}$) as a function of irradiation temperature. The results are deduced from Fig. 4(f) by subtracting the defect density in NP Au from the defect density in CG Au irradiated at the same temperature. Below 200 °C, $\rho_{\rm absorb}^{\rm NP}$ decreases slightly (from 11.5 to 10.5 × 10²²/m³) with increasing temperature. However, when T > 200 °C, $\rho_{\rm absorb}^{\rm NP}$ decreases sharply with increasing temperature. (b) Calculated nanopore effective sink strength for defect clusters as a function of irradiation temperature. The shadowed area represents the deviation by considering the variation of nanopore size. Clearly, two distinct regions can be identified. Below 200 °C (Region I), effective sink strength is inversely proportional to irradiation temperature.

and (3) the recombination of interstitials and vacancies.

One may speculate that the shrinkage of nanopores could be caused by the surface diffusion of Au atoms at elevated temperatures. However, we have performed the annealing studies on NP Au at 400 °C for 20 min, and nanopores were very stable during annealing (Supplementary Fig. S1). In addition, irradiation resistance of NP metals may degrade over long-term irradiation when most of the nanopores are completely filled by irradiation-induced defect clusters. Therefore, the stability of nanopores should also be considered if NP materials are adopted to design irradiation-

resistant materials in nuclear reactors. First, nanopores in Au appear to shrink at a fast speed at lower temperatures, for instance, ~10%/dpa at 200 °C. However, Au is a model system that is known to be vulnerable to irradiation damage than many other alloys. Thus, one can envision that if practical reactor steels are engineered into nanoporous structures, the safe service period (lifetime) of the steels could be significantly extended. Second, the stability of nanopores increases at high temperatures. For instance, the nanopore shrinkage rate at 400 °C decreases to less than 2%/dpa. This is instrumental for NP metals because the nuclear reactors are usually

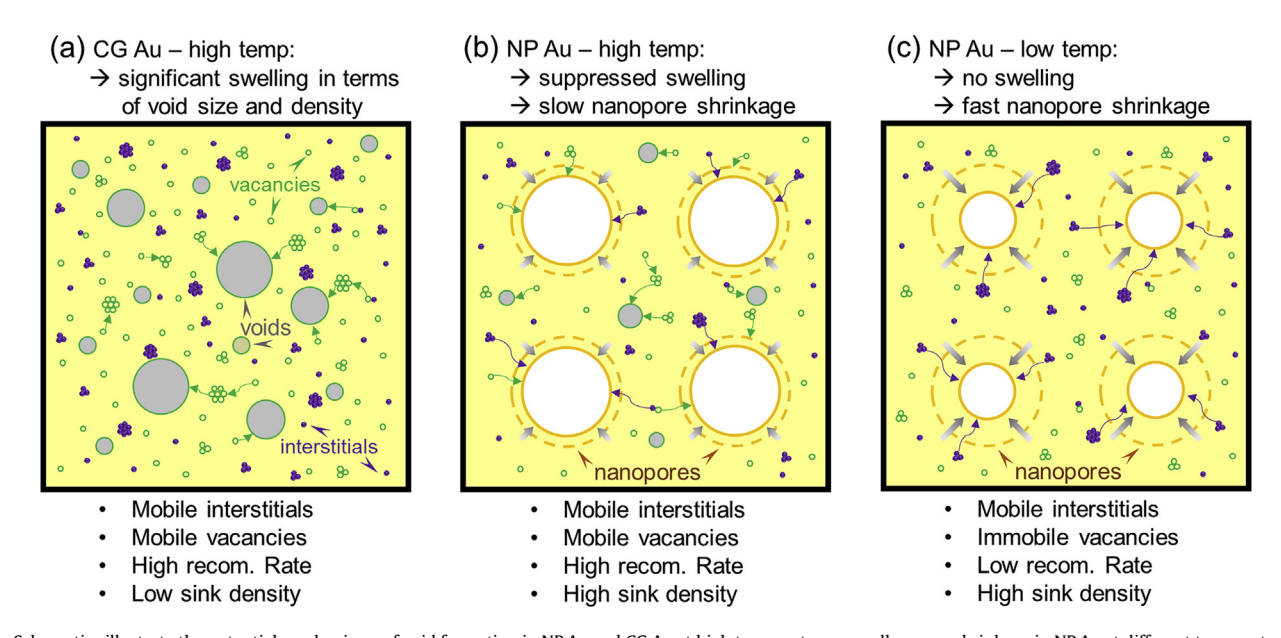


Fig. 11. Schematics illustrate the potential mechanisms of void formation in NP Au and CG Au at high temperature as well as pore shrinkage in NP Au at different temperatures after irradiation. As irradiation condition is identical, the defect generation rate is assumed to be identical between CG and NP Au. (a) In CG Au irradiated at high temperature, due to a lack of internal defect sinks, interstitials rapidly migrate away, leaving vacancies behind. The supersaturation of vacancies leads to the formation of voids. (b) In contrast in NP Au irradiated at high temperature, both interstitials and vacancies are trapped by nanopores. As the migration rate and territory of interstitials are curtailed by nanopores, the recombination probability of vacancies and interstitials may also increase. Consequently, only small vacancy clusters can form, and the magnitude of void swelling significantly decreases. (c) Comparing to NP Au irradiated at high temperature, nanopores shrinkage rates increases at lower irradiation temperature presumably because less thermal recombination of vacancies and interstitials at low temperature, and absorption of interstitials by nanopores.

operated at temperatures above 400 °C. Third, the stability can also be increased by increasing the size of nanopores. As discussed previously [46], the shrinking rate of nanopores is size-dependent, i.e., nanopore shrinkage is inversely proportional to the initial pore diameter. Of course, irradiation response of other NP metals may be different from NP Au reported in this study. However, the concept provided here is potentially transformative. For instance, the introduction of nanopores can clearly reduce irradiation induced defect density and nanopores shrinkage rate decreases at elevated temperatures. Therefore, by deliberately introducing nanopores with desired dimensions, the irradiation stability of NP metals can be significantly sustained. These observations may have general implications for the design of advanced irradiation resistant metallic materials.

In addition to the irradiation stability of nanopores, further investigations on other properties, such as mechanical properties, resistance to corrosion, are beneficial to transfer this concept into a practical option for advanced reactor materials.

5. Conclusion

Nanoporous (NP) materials possess a great potential in the alleviation of the irradiation-induced damage due to the giant surface-to-volume ratio. In this study, we show that both defect size and density evolve with irradiation temperature, i.e., hightemperature results in reduced defect size and density. Compared to CG Au, defect size and density have been markedly reduced in NP Au. In addition, nanopore shrinkage has been identified at all temperatures, and shrinkage rate becomes less at high temperatures. The sink strength of the free surface (nanopores) in NP Au is estimated. The method used in this study not only offers an opportunity for quantitatively analyzing sink strength but more importantly, but also provides a new strategy to make crosswise comparisons of sink strength between different defect sinks. The significantly enhanced swelling resistance of NP metals empowers them as promising candidates as structural materials for advanced nuclear reactors.

Acknowledgement

We acknowledge financial support by NSF-CMMI under grant no. 1728419. HW acknowledges the support from the U.S. Office of Naval Research (N00014-16-1-2778). We also acknowledge the use of microscopes at the Microscopy and Imaging Center at Purdue University. This work was performed, in part, at the Center for Integrated Nanotechnologies, an Office of Science User Facility operated for the U.S. Department of Energy (DOE) Office of Science by Los Alamos National Laboratory (Contract DE-AC52-06NA25396) and Sandia National Laboratories (Contract DE-NA-0003525). The IVEM facility at Argonne National Laboratory is supported by DOE-Office of Nuclear Energy.

Appendix A. Supplementary data

Supplementary data related to this article can be found at https://doi.org/10.1016/j.actamat.2017.09.054.

References

- S.J. Zinkle, 1.03-Radiation-Induced effects on microstructure, in: A2-Konings, J.M. Rudy (Eds.), Comprehensive Nuclear Materials, Elsevier, Oxford, 2012, pp. 65–98.
- [2] G.S. Was, Fundamental of Radiation Materials Science: Metals and Alloys, Springer, New York, 2007, p. 827.
- [3] L.K. Mansur, E.E. Bloom, Radiation effects in reactor structural alloys, JOM 34 (10) (1982) 23–31.

- [4] C. Baroch (Ed.), Properties of Reactor Structural Alloys after Neutron or Particle Irradiation, STP570-EB, ASTM International, West Conshohocken, PA, 1975.
- [5] S.J. Zinkle, Materials Issues for Generation IV System, Springer, Netherlands, 2008, pp. 227–244.
- [6] J.L. Boutard, S. Dudarev, E. Diegele, Materials Issues for Generation IV Systems, Springer Netherlands 481–500.
- [7] S.J. Zinkle, L.E. Seitzman, W.G. Wolfer, I. Energy calculations for pure metals, Philos. Mag. A 55 (1) (1987) 111–125.
- [8] B.N. Singh, S.J. Zinkle, Defect accumulation in pure fcc metals in the transient regime: a review, J. Nucl. Mater. 206 (2) (1993) 212–229.
- [9] B.N. Singh, S.I. Golubov, H. Trinkaus, D.J. Edwards, M. Eldrup, Review: evolution of stacking fault tetrahedra and its role in defect accumulation under cascade damage conditions, J. Nucl. Mater. 328 (2–3) (2004) 77–87.
- [10] D.J. Bacon, T. Diaz de la Rubia, Molecular dynamics computer simulations of displacement cascades in metals, J. Nucl. Mater. 216 (1994) 275–290.
- [11] C.-C. Fu, J.D. Torre, F. Willaime, J.-L. Bocquet, A. Barbu, Multiscale modelling of defect kinetics in irradiated iron, Nat. Mater 4 (1) (2005) 68–74.
 [12] B.P. Uberuaga, R.G. Hoagland, A.F. Voter, S.M. Valone, Direct transformation of
- [12] B.P. Uberuaga, R.G. Hoagland, A.F. Voter, S.M. Valone, Direct transformation of vacancy voids to stacking fault tetrahedra, Phys. Rev. Lett. 99 (13) (2007) 135501.
- [13] R.E. Stoller, G.R. Odette, B.D. Wirth, Primary damage formation in bcc iron, J. Nucl. Mater. 251 (1997) 49–60.
- [14] G.R. Odette, M.J. Alinger, B.D. Wirth, Recent developments in irradiation-resistant steels. Annu. Rev. Mater. Res. 38 (1) (2008) 471–503.
- [15] L.K. Mansur, A.F. Rowcliffe, R.K. Nanstad, S.J. Zinkle, W.R. Corwin, R.E. Stoller, Materials needs for fusion, Generation IV fission reactors and spallation neutron sources – similarities and differences, J. Nucl. Mater. 329–333 (2004) 166–172.
- [16] S.J. Zinkle, Fusion materials science: overview of challenges and recent progress, Phys. Plasmas 12 (5) (2005) 058101.
- [17] R.W. Grimes, R.J.M. Konings, L. Edwards, Greater tolerance for nuclear materials, Nat. Mater. 7 (9) (2008) 683–685.
- [18] K.Y. Yu, Y. Chen, J. Li, Y. Liu, H. Wang, M.A. Kirk, M. Li, X. Zhang, Measurement of heavy ion irradiation induced in-plane strain in patterned face-centered-cubic metal films: an in situ study, Nano Lett. 16 (12) (2016) 7481–7489.
- [19] S. Kashibe, K. Une, K. Nogita, Formation and growth of intragranular fission gas bubbles in UO 2 fuels with burnup of 6–83 GWd/t, J. Nucl. Mater. 206 (1) (1993) 22–34
- [20] J. Turnbull, The distribution of intragranular fission gas bubbles in UO2 during irradiation, J. Nucl. Mater. 38 (2) (1971) 203–212.
- [21] K. Une, K. Nogita, S. Kashibe, M. Imamura, Microstructural change and its influence on fission gas release in high burnup UO2 fuel, J. Nucl. Mater. 188 (1992) 65–72.
- [22] M. Verwerft, Multiple voltage electron probe microanalysis of fission gas bubbles in irradiated nuclear fuel, J. Nucl. Mater. 282 (2) (2000) 97–111.
- [23] G.L. Hofman, Y.S. Kim, A classification of uniquely different types of nuclear fission gas behavior, Nucl. Eng. Technol. 37 (4) (2005) 299–308.
- [24] M.P. Surh, J.B. Sturgeon, W.G. Wolfer, Void nucleation, growth, and coalescence in irradiated metals, J. Nucl. Mater. 378 (1) (2008) 86–97.
- [25] S.F. Pugh, Voids formed by irradiation of reactor materials report of conference, J. Br. Nucl. Energy Soc. 10 (3) (1971) 159.
- [26] S.F. Pugh, Radiation induced voids in metals report on usaec conference, J. Br. Nucl. Energy Soc. 11 (1) (1972) 9.
- [27] D.I.R. Norris, Voids in irradiated metals (Part I), Radiat. Eff. 14 (1–2) (1972) 1–37.
- [28] D.I.R. Norris, Voids in irradiated metals (Part II), Radiat. Eff. 15 (1-2) (1972) 1-22.
- [29] Q. Guo, P. Landau, P. Hosemann, Y. Wang, J.R. Greer, Helium implantation effects on the compressive response of Cu nanopillars, Small 9 (5) (2013) 691–696.
- [30] R. Liontas, X.W. Gu, E. Fu, Y. Wang, N. Li, N. Mara, J.R. Greer, Effects of helium implantation on the tensile properties and microstructure of Ni73P27 metallic glass Nanostructures, Nano Lett. 14 (9) (2014) 5176–5183.
- [31] M. Caro, W.M. Mook, E.G. Fu, Y.Q. Wang, C. Sheehan, E. Martinez, J.K. Baldwin, A. Caro, Radiation induced effects on mechanical properties of nanoporous gold foams, Appl. Phys. Lett. 104 (23) (2014) 233109.
- [32] S.A. Maloy, M.R. James, G. Willcutt, W.F. Sommer, M. Sokolov, L.L. Snead, M.L. Hamilton, F. Garner, The mechanical properties of 316L/304L stainless steels, Alloy 718 and Mod 9Cr-1Mo after irradiation in a spallation environment, J. Nucl. Mater. 296 (1-3) (2001) 119-128.
- [33] Y. Chen, Y. Liu, E.G. Fu, C. Sun, K.Y. Yu, M. Song, J. Li, Y.Q. Wang, H. Wang, X. Zhang, Unusual size-dependent strengthening mechanisms in helium ionirradiated immiscible coherent Cu/Co nanolayers, Acta Mater. 84 (2015) 393—404.
- [34] K.Y. Yu, D. Bufford, C. Sun, Y. Liu, H. Wang, M.A. Kirk, M. Li, X. Zhang, Removal of stacking-fault tetrahedra by twin boundaries in nanotwinned metals, Nat. Commun. 4 (2013) 1377.
- [35] M.J. Demkowicz, A. Misra, A. Caro, The role of interface structure in controlling high helium concentrations, Curr. Opin. Solid State Mater. Sci. 16 (3) (2012) 101–108.
- [36] Q.M. Wei, N. Li, N. Mara, M. Nastasi, A. Misra, Suppression of irradiation hardening in nanoscale V/Ag multilayers, Acta Mater. 59 (16) (2011) 6331–6340.
- [37] K.Y. Yu, Z. Fan, Y. Chen, M. Song, Y. Liu, H. Wang, M.A. Kirk, M. Li, X. Zhang, In situObservation of defect annihilation in Kr ion-irradiated bulk Fe/

- Amorphous-Fe2Zr nanocomposite alloy, Mater. Res. Lett. 3 (1) (2014) 35-42.
- [38] J. Li, Y. Chen, H. Wang, X. Zhang, In situ studies on twin-thickness-dependent distribution of defect clusters in heavy ion-irradiated nanotwinned Ag, Metall. Mater. Trans. A 48 (3) (2017) 1466—1473.
- [39] Y. Chen, J. Li, K.Y. Yu, H. Wang, M.A. Kirk, M. Li, X. Zhang, In situ studies on radiation tolerance of nanotwinned Cu, Acta Mater. 111 (2016) 148–156.
- [40] Y. Chen, N. Li, D.C. Bufford, J. Li, K. Hattar, H. Wang, X. Zhang, In situ study of heavy ion irradiation response of immiscible Cu/Fe multilayers, J. Nucl. Mater. 475 (2016) 274–279.
- [41] J. Li, K.Y. Yu, Y. Chen, M. Song, H. Wang, M.A. Kirk, M. Li, X. Zhang, In situ study of defect migration kinetics and self-healing of twin boundaries in heavy ion irradiated nanotwinned metals, Nano Lett. 15 (5) (2015) 2922–2927.
- [42] C. Sun, B.P. Uberuaga, L. Yin, J. Li, Y. Chen, M.A. Kirk, M. Li, S.A. Maloy, H. Wang, C. Yu, X. Zhang, Resilient ZnO nanowires in an irradiation environment: an in situ study, Acta Mater. 95 (2015) 156–163.
- [43] E.M. Bringa, J.D. Monk, A. Caro, A. Misra, L. Zepeda-Ruiz, M. Duchaineau, F. Abraham, M. Nastasi, S.T. Picraux, Y.Q. Wang, D. Farkas, Are nanoporous materials radiation resistant? Nano Lett. 12 (7) (2012) 3351–3355.
- [44] C. Sun, D. Bufford, Y. Chen, M.A. Kirk, Y.Q. Wang, M. Li, H. Wang, S.A. Maloy, X. Zhang, In situ study of defect migration kinetics in nanoporous Ag with enhanced radiation tolerance, Sci. Rep. 4 (2014) 3737.
- [45] E.J. Kosiancic, Method of making porous nuclear fuel, Google Patents, 1977.
- [46] J. Li, C. Fan, J. Ding, S. Xue, Y. Chen, Q. Li, H. Wang, X. Zhang, In situ heavy ion irradiation studies of nanopore shrinkage and enhanced radiation tolerance of nanoporous Au, Sci. Rep. 7 (2017) 39484.
- [47] E.G. Fu, M. Caro, L.A. Zepeda-Ruiz, Y.Q. Wang, K. Baldwin, E. Bringa, M. Nastasi, A. Caro, Surface effects on the radiation response of nanoporous Au foams, Appl. Phys. Lett. 101 (19) (2012) 191607.
- [48] Y. Chen, K.Y. Yu, Y. Liu, S. Shao, H. Wang, M.A. Kirk, J. Wang, X. Zhang, Damage-tolerant nanotwinned metals with nanovoids under radiation environments, Nat. Commun. 6 (2015) 7036.
- [49] C. Jiang, N. Swaminathan, J. Deng, D. Morgan, I. Szlufarska, Effect of grain boundary stresses on sink strength, Mater. Res. Lett. 2 (2) (2013) 100–106.
- boundary stresses on sink strength, Mater. Res. Lett. 2 (2) (2013) 100–106 [50] G.S. Was, Was, Fundamentals of Radiation Materials Science, 2007.
- [51] A.H. King, D.A. Smith, Calculations of sink strength and bias for point-defect absorption by dislocations in arrays, Radiat. Eff. 54 (3-4) (2006) 169-176.
- [52] S. Kondo, Y. Katoh, L.L. Snead, Analysis of grain boundary sinks and interstitial diffusion in neutron-irradiated SiC, Phys. Rev. B 83 (7) (2011).
- [53] J. Burke, D. Stuckey, Dislocation loop-free zones around grain boundaries in quenched aluminium and aluminium alloys, Philos. Mag. 31 (5) (1975) 1063–1080.
- [54] B.N. Singh, A.J.E. Foreman, Calculated grain size-dependent vacancy supersaturation and its effect on void formation, Philos. Mag. 29 (4) (1974) 847–858.
- [55] W.Z. Han, M.J. Demkowicz, E.G. Fu, Y.Q. Wang, A. Misra, Effect of grain boundary character on sink efficiency, Acta Mater. 60 (18) (2012) 6341–6351.
- [56] C. Jiang, N. Swaminathan, J. Deng, D. Morgan, I. Szlufarska, Effect of grain boundary stresses on sink strength, Mater. Res. Lett. 2 (2) (2014) 100–106.
- [57] Y. Zhang, H. Huang, P.C. Millett, M. Tonks, D. Wolf, S.R. Phillpot, Atomistic study of grain boundary sink strength under prolonged electron irradiation, J. Nucl. Mater. 422 (1–3) (2012) 69–76.
- [58] L. Malerba, C.S. Becquart, C. Domain, Object kinetic Monte Carlo study of sink strengths, J. Nucl. Mater. 360 (2) (2007) 159–169.
- [59] A.M. Monti, A. Sarce, N. Smetniansky-De Grande, E.J. Savino, C.N. Tomé, Point defects and sink strength in h.c.p. metals, Philos. Mag. A 63 (5) (1991) 925–936.
- [60] B.P. Uberuaga, L.J. Vernon, E. Martinez, A.F. Voter, The relationship between grain boundary structure, defect mobility, and grain boundary sink efficiency, Sci. Rep. 5 (2015) 9095.
- [61] M.A. Tschopp, K.N. Solanki, F. Gao, X. Sun, M.A. Khaleel, M.F. Horstemeyer, Probing grain boundary sink strength at the nanoscale: energetics and length scales of vacancy and interstitial absorption by grain boundaries inα-Fe, Phys. Rev. B 85 (6) (2012).
- [62] M.J. Demkowicz, R.G. Hoagland, B.P. Uberuaga, A. Misra, Influence of interface sink strength on the reduction of radiation-induced defect concentrations and fluxes in materials with large interface area per unit volume, Phys. Rev. B 84

- (10) (2011) 104102.
- [63] K.Y. Yu, C. Sun, Y. Chen, Y. Liu, H. Wang, M.A. Kirk, M. Li, X. Zhang, Superior tolerance of Ag/Ni multilayers against Kr ion irradiation: an in situ study, Philos. Mag. 93 (26) (2013) 3547–3562.
- [64] M.J. Demkowicz, The influence of Sigma 3 twin boundaries on the formation of radiation-induced defect clusters in nanotwinned Cu, J. Mater. Res. 26 (14) (2011) 1666–1675.
- [65] Y.N. Osetsky, D.J. Bacon, Defect cluster formation in displacement cascades in copper, Nucl. Instrum. Meth. Phys. Res. Sect. B Beam Interact. Mater. Atoms 180 (1–4) (2001) 85–90.
- [66] S.J. Zinkle, Y. Matsukawa, Observation and analysis of defect cluster production and interactions with dislocations, J. Nucl. Mater. 329–333 (1–3 PART A) (2004) 88–96.
- [67] J. Silcox, P.B. Hirsch, Direct observations of defects in quenched gold, Philos. Mag. 4 (37) (1959) 72–89.
- [68] Y. Matsukawa, S.J. Zinkle, One-dimensional fast migration of vacancy clusters in metals, Science 318 (5852) (2007) 959–962.
- [69] T. Kadoyoshi, H. Kaburaki, F. Shimizu, H. Kimizuka, S. Jitsukawa, J. Li, Molecular dynamics study on the formation of stacking fault tetrahedra and unfaulting of Frank loops in fcc metals, Acta Mater. 55 (9) (2007) 3073–3080.
- [70] Y.N. Osetsky, D.J. Bacon, A. Serra, B.N. Singh, S.I. Golubov, Stability and mobility of defect clusters and dislocation loops in metals, J. Nucl. Mater. 276 (1–3) (2000) 65–77.
- [71] J.W. Corbett, in: James W. Corbett (Ed.), Electron Radiation Damage in Semiconductors and Metals, Academic Press, New York, 1966.
- [72] B.L. Eyre, Transmission electron microscope studies of point defect clusters in fcc and bcc metals, J. Phys. F Met. Phys. 3 (2) (1973) 422.
- [73] N. Hashimoto, T.S. Byun, K. Farrell, S.J. Zinkle, Deformation microstructure of neutron-irradiated pure polycrystalline metals, J. Nucl. Mater. 329–333 (Part B) (2004) 947–952.
- [74] B.N. Singh, M. Eldrup, S.J. Zinkle, S.I. Golubov, On grain-size-dependent void swelling in pure copper irradiated with fission neutrons, Philos. Mag. A 82 (6) (2002) 1137–1158.
- [75] Y. Dai, M. Victoria, Defect structures in deformed f.c.c. metals, Acta Mater. 45 (8) (1997) 3495–3501.
- [76] B.N. Singh, D.J. Edwards, A. Horsewell, P. Toft, Dose Dependence of Microstructural Evolution and Mechanical Properties of Neutron Irradiated Copper and Copper Alloys, Denmark, 1995, p. 34.
- [77] J.W. Muncie, B.L. Eyre, C.A. English, Low-dose neutron irradiation damage in copper. I. Vacancy loop production, Philos. Mag. A 52 (3) (1985) 309–331.
- [78] K. Arakawa, K. Ono, M. Isshiki, K. Mimura, M. Uchikoshi, H. Mori, Observation of the one-dimensional diffusion of nanometer-sized dislocation loops, Science 318 (5852) (2007) 956–959.
- [79] Jin Li, Y. Chen, H. Wang, X. Zhang, In situ study on enhanced heavy ion irradiation tolerance of porous Mg, Scr. Mater. (2017) in press.
- [80] C. Fan, Y. Chen, Jin Li, Jie Ding, H. Wang, X. Zhang, Defect evolution in heavy ion irradiated nanotwinned Cu with nanovoids, J. Nuclear Mater. (2017) in
- [81] C. Fan, Jin Li, Z. Fan, H. Wang, X. Zhang, In Situ studies on the irradiationinduced twin boundary-defect interactions in Cu, Metall. Mater. Trans. A (2017) 1–9.
- [82] J. Li, C. Fan, J. Ding, S. Xue, Y. Chen, Q. Li, H. Wang, X. Zhang, In situ heavy ion irradiation studies of nanopore shrinkage and enhanced radiation tolerance of nanoporous Au, Sci. Rep 7 (2017) 39484.
- [83] Cuiling Li, Hongjing Wang, Yusuke Yamauchi, Electrochemical deposition of mesoporous Pt—Au alloy films in aqueous surfactant solutions: towards a highly sensitive amperometric glucose sensor, Chem. Euro. J. 19 (February 11, 2013) 2242–2246.
- [84] C. Li, Ö. Dag, T.D. Dao, T. Nagao, Y. Sakamoto, T. Kimura, O. Terasaki, Y. Yamauchi, Electrochemical synthesis of mesoporous gold films toward mesospace-stimulated optical properties, Nat. Commun. 6 (2015 Mar 23) 6608, https://doi.org/10.1038/ncomms7608.
- [85] V. Malgras, H. Ataee-Esfahani, H. Wang, B. Jiang, C. Li, K.C. Wu, J.H. Kim, Y. Yamauchi, Nanoarchitectures for mesoporous metals, Adv. Mater. 28 (6) (February 10, 2016) 993–1010.